Low-Resolution Self-Attention for Semantic Segmentation

Yu-Huan Wu, Shi-Chen Zhang, Yun Liu, Le Zhang, Xin Zhan, Daquan Zhou, Jiashi Feng, Ming-Ming Cheng, and Liangli Zhen

Abstract—Semantic segmentation tasks naturally require high-resolution information for pixel-wise segmentation and global context information for class prediction. While existing vision transformers demonstrate promising performance, they often utilize high-resolution context modeling, resulting in a computational bottleneck. In this work, we challenge conventional wisdom and introduce the Low-Resolution Self-Attention (LRSA) mechanism to capture global context at a significantly reduced computational cost, *i.e.*, FLOPs. Our approach involves computing self-attention in a fixed low-resolution space, regardless of the input image's resolution, with additional 3×3 depth-wise convolutions to capture fine details in the high-resolution space. We demonstrate the effectiveness of our LRSA approach by building the LRFormer, a vision transformer with an encoder-decoder structure. Extensive experiments on the ADE20K, COCO-Stuff, and Cityscapes datasets demonstrate that LRFormer outperforms state-of-the-art models. Code is available at https://github.com/yuhuan-wu/LRFormer.

Index Terms—Low-Resolution Self-Attention, Semantic Segmentation, Vision Transformer

1 Introduction

As a fundamental computer vision problem, semantic segmentation [1]–[3] aims to assign a semantic label to each image pixel. Semantic segmentation models [4], [5] usually rely on pretrained backbone networks [6], [7] for feature extraction, which is then followed by specific designs for pixel-wise predictions. In the last decade, the progress in feature extraction via various backbone networks has consistently pushed forward state-of-the-art semantic segmentation [8]–[10]. This paper improves the feature extraction for semantic segmentation from a distinct perspective.

It is commonly believed that semantic segmentation, as a dense prediction task, requires high-resolution features to ensure accuracy. In contrast, image classification typically infers predictions from a very small feature map, such as 1/32 of the input resolution. Semantic segmentation models with convolutional neural networks (CNNs) usually decrease the strides of backbone networks to increase the feature resolution [11]–[14], *e.g.*, 1/8 of the input resolution. This attribute is also well preserved in transformer-based semantic segmentation, demonstrating that high-resolution is still necessary for semantic segmentation.

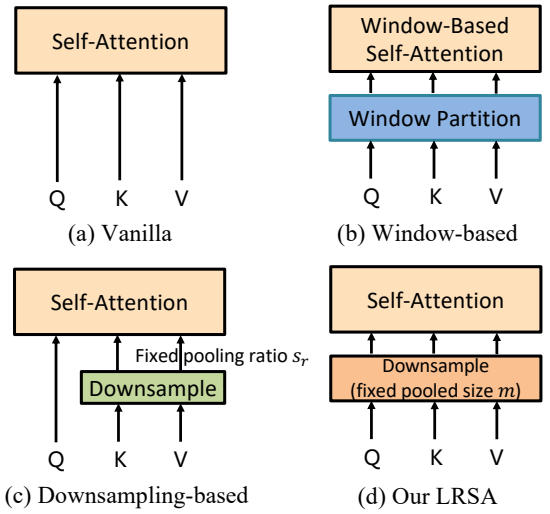

Fig. 1. **Comparison of existing and our proposed paradigms for the self-attention calculation in the vision transformer**. Representatives include (a) ViT [15], DeiT [16]; (b) Swin [17], CSwin [18]; (c) PVT [19], SegFormer [9], P2T [20]; and (d) our LRFormer. Positional encoding modules are not drawn in this module. More details of (d) can refer to Fig. 3.

High-resolution features are powerful for capturing the local details, while context information pertains to the broader understanding of the scene. Contextual features discern the interrelations between various scene components [21], mitigating the ambiguity inherent in local features. Thus, considerable research efforts [1], [22] have been devoted to extending the receptive field of CNNs. Conversely, vision transformers inherently facilitate the computation of global relationships by introducing self-attention with a global receptive field. Nonetheless, this comes at a significant computational cost, as vanilla attention mechanisms exhibit

- *Y.-H. Wu was with Nankai University when he started this research. Y.-H. Wu and L. Zhen are currently with the Institute of High Performance Computing (IHPC), A*STAR, Singapore. (E-mail: wyh.nku@gmail.com, llzhen@outlook.com)*
- *S.-C. Zhang, Y. Liu, and M.-M. Cheng are with NKIARI, Shenzhen Futian and VCIP, Nankai University, Tianjin, China. (E-mail: zhangshichen@mail.nankai.edu.cn, liuyun@nankai.edu.cn, and cmm@nankai.edu.cn)*
- *L. Zhang is with the University of Electronic Science and Technology of China. (E-mail: zhangleuestc@gmail.com)*
- *X. Zhan is with Udeer AI, Hangzhou, China. (E-mail: zhanxin@udeer.ai)*
- *D. Zhou is with School of Electronic and Computer Engineering, Peking University, China. (E-mail: zhoudaquan21@gmail.com)*
- *J. Feng is with Bytedance Inc., Singapore. (E-mail: jshfeng@bytedance.com)*
- *M.-M. Cheng is the corresponding author.*

quadratic complexity to input length. Intriguingly, seminal studies [9], [20], [23] made a remarkable effort by judiciously downsampling some of the features (*i.e.*, key and value) during the self-attention computation for reduced computational complexities.

Nevertheless, we observe that the computational overhead of self-attention remains a non-negligible bottleneck for existing vision transformers, as evidenced by Tab. 12. Consequently, we aim to delve deeper into the downsampling in the core component of the transformer, *i.e.*, self-attention. Diverging from prior works that only downsample the key and value features [9], [20], [23], we propose to downsample all constituents—query, key, and value features. In this way, the output of self-attention would be in a low-resolution so that the mainstream of the transformer would contain low-resolution. Furthermore, we adopt a fixed downsampling size rather than a downsampling ratio to attain a very low computational complexity for self-attention. The proposed method is called **Low-Resolution Self-Attention (LRSA)**.

Fig. 1 depicts the differences between existing self-attention approaches and our LRSA. Vanilla self-attention [15] (Fig. 1(a)) directly computes the global feature relations in the original resolution, which is quite expensive. Window-based methods [17], [18], [24], [25] (Fig. 1(b)) divide the features into small windows and perform local self-attention within each window. Downsampling-based methods [9], [19], [20], [26] (Fig. 1(c)) keep the size of the query unchanged, and they downsample the key and value features with a fixed pooling ratio. The lengths of key and value features increase linearly with the input resolution. In contrast, our LRSA (Fig. 1(d)) downsamples all query, key, and value to a small fixed size, leading to very low complexity regardless of the input resolution. More analysis of the computational complexity can refer to §3.1.

While LRSA significantly boosts efficiency in capturing global context, we recognize that maintaining fine-grained details is another critical aspect for optimal performance in semantic segmentation. To address this duality, we employ LRSA to capture global context information in a purely low-resolution domain, while simultaneously integrating small kernel (3×3) depth-wise convolution to capture local details in the high-resolution space. Based on these foundational principles, we build a new backbone network for feature extraction and a simple decoder to aggregate the extracted multi-level features for semantic segmentation. This new model is dubbed as **Low-Resolution Transformer (LRFormer)**. We evaluate LRFormer on popular benchmarks, including ADE20K [27], COCO-Stuff [28], and Cityscapes [29]. Experimental results (*e.g.*, Fig. 2) demonstrate the superiority of LRFormer series over state-of-the-art models.

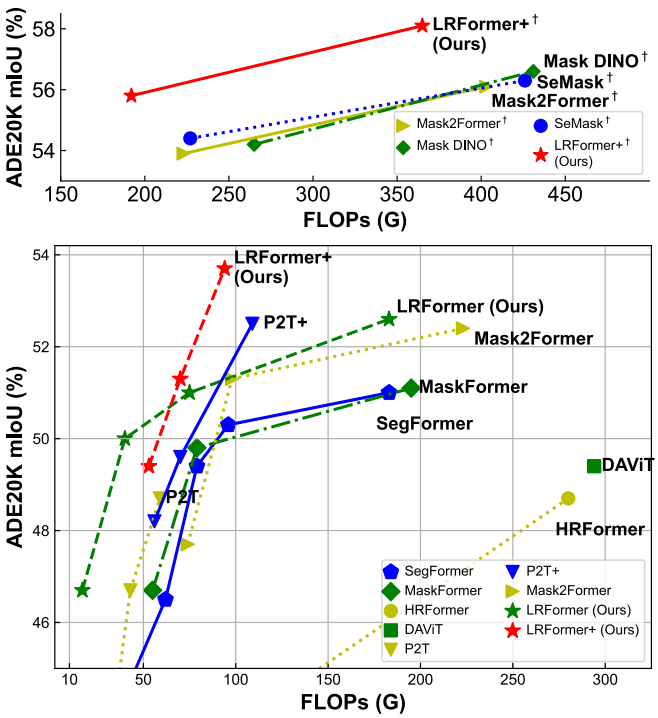

Fig. 2. **Experimental comparisons on ADE20K [27] dataset.** Methods marked with "†" are the results pretrained on the ImageNet-22K dataset. Data are from Tab. 3 and Tab. 13.

2 Related Work

2.1 Semantic Segmentation

Semantic segmentation is a fundamental task in computer vision. It is challenging due to the numerous variations like object sizes, textures, and lighting conditions in practical scenarios. FCN [30], the pioneering work in this area, proposed the adaptation of CNNs for semantic segmentation in an end-to-end manner. Since then, numerous studies have been built upon FCN [30], with major efforts focused on enriching multi-scale representations [4], [5], [31], enhancing boundary perception [32]–[35], contextual representations [21], [36] and introducing visual attention [2], [3], [8], [11], [14]. These studies deeply explored the semantic head design upon FCN [30] and achieved great progress. Among these, many approaches [1]–[5], [8], [11]–[14], [37]–[39] are greatly benefited from the high-resolution features, performing prediction in the 1/8 of the input resolution to ensure high accuracy. Moreover, there exist some query-based frameworks [40]–[42], [42]–[45] that changed the decoder style in semantic segmentation. For example, Panoptic SegFormer [40] introduced a unified mask prediction workflow using a query decoupling strategy to handle thing and stuff categories separately. MaskFormer [41] revolutionized mask decoders with transformer-based mask classification. Mask2Former [42] significantly enhanced MaskFormer via multi-scale masked attention. K-Net [43] unifies various segmentation tasks through dynamic kernels. K-means Transformer [44] integrated K-means clustering to optimize the mask generation for better instance

More recently, many works [9], [10], [41], [42], [46] showed that vision transformers [15] can largely improve the performance of semantic segmentation. This is mainly attributed to the strong global capability of vision transformers, which happens to be a crucial property required for semantic segmentation. For example, SETR [46] first adapted ViT as an encoder followed by multi-level feature aggregation. SegFormer [9] introduced a novel pyramid vision transformer encoder with an MLP mask decoder. FeedFormer [47] introduced a transformer-based decoder with features as queries, significantly enhancing the structure information. More discussions on vision transformers can refer to §2.3.

Recently, there exist some universal or foundational vision models exploring large scale capabilities, such as EVA [48], OneFormer [49], and One-Peace [50]. They also achieved a great success in semantic segmentation due to their superior capability, some of which are even very capable to process multi-modal input. For clarity, we are not able to compare our LRFormer with these large vision models due to limited GPU resources currently.

2.2 Convolutional Neural Networks

Given that CNN-based semantic segmentation models rely on CNN backbones for feature extraction, we discuss some notable CNN architectures. Since the emergence of AlexNet [51], many techniques have been developed to strengthen the CNN representations and achieved great success. For example, VGG [52], GoogleNet [53], ResNets [6] and DenseNets [54] developed increasingly deep CNNs to learn more powerful representations. ResNeXts [7], Res2Nets [55], and ResNeSts [56] explored the cardinal design in ResNets [6]. SENet [57] and SKNet [58] introduced different attention architectures for selective feature learning. Very recently, CNNs with large kernels are proven powerful in some works [59]–[61]. To ensure the high-resolution of feature maps for accurate semantic segmentation, semantic segmentation models usually decrease the strides of these CNNs and uses the dilated convolutions [22] to keep larger receptive field. Motivated by this, HRNet [62] was proposed to directly learn high-resolution CNN features. Despite the numerous successful stories, CNNs are limited in capturing global and long-range relationships, which are of vital importance for semantic segmentation.

2.3 Vision Transformers

Transformers are initially proposed in natural language processing (NLP) [63]. Through multi-head self-attention (MHSA), transformers are capable of modeling global relationships. Thanks to this characteristic, transformers may also be powerful for computer vision tasks that require global information for a whole understanding of the visual scenarios. To bridge this gap, ViT [15] transformed an image to tokens via a 16×16 pooling operation and adopts the transformer to process these tokens, achieving better performance than CNNs in image recognition. After that, vision transformers are developed rapidly by leveraging knowledge distillation [64], overlapping patch embedding [65] or convolutions [66], [67]. Recently, pyramid vision transformers [10], [17], [19], [20], [23], [26], [68], [69] are proven to be powerful for image recognition tasks like semantic segmentation. For example, PVT [19] and MViT [26] proposed to build a pyramid vision transformer pipeline via performing downsampling on key and value features. Notably, MViT [26] decreases the resolution of the query by half in the first block of each stage, without the need of patch embedding between each stage. Liu *et al.* [17] created a window-based vision transformer with shifted windows. Yuan *et al.* [10] presented HRFormer to learn high-resolution features for dense prediction using the vision transformer. Xia *et al.* [70] proposed DAT with deformable attention, conducting deformable sampling on key and value features. Wu *et al.* [20] introduced an efficient and multi-scale self-attention strategy via in-layer pyramid pooling. Liu *et al.* [71] proposed to compute the self-attention in a hierarchical manner. More approaches can refer to the survey [72].

TABLE 1
Comparison of various self-attention schemes. N is the length of the flattened features and C is the number of feature channels. "Spatial Corr." denotes the spatial correlation. We omit constant factors for simplicity, like the window size in window-based methods and the downsampled size of LRSA.

Scheme	Global	Spatial Corr.	Complexity
Window-based [17]	✘	✔	$O(NC^2)$
Factorized [73]	✔	✘	$O(NC^2)$
Downsampling-based [9]	✔	✔	$O(N^2C + NC^2)$
LRSA (Ours)	✔	✔	$O(NC + C^2)$

Despite their reported effectiveness, it is still commonly believed that high-resolution features are crucial for self-attention to effectively capture contextual information in semantic segmentation. Window-based vision transformers [17], [18], [24], [25] calculate self-attention within each local windows to reduce the computational complexity so that they can keep the high-resolution of feature maps. Downsampling-based vision transformers [9], [19], [20], [23], [26], [71] keep the size of the query while partially conduct the downsampling on the key and value features with a fixed pooling ratio. Such strategy greatly reduces the complexity compared with vanilla attention so as to keep high-resolution features, making themselves computationally non-negligible especially for high-resolution inputs (Tab. 12). In contrast, we question the necessity of keeping high-resolution for capturing context information via self-attention. We study this question by proposing LRFormer with LRSA. The good performance on several public benchmarks suggest the superiority of our LRFormer for semantic segmentation.

3 Methodology

In this section, we first introduce the Low-Resolution Self-Attention (LRSA) mechanism in §3.1. Then, we build Low-Resolution Transformer (LRFormer) using LRSA for semantic segmentation in §3.2. The decoder of LRFormer is presented in §3.3. Finally, we provide the implementation details in §3.4.

3.1 Low-Resolution Self-Attention

Unlike existing vision transformers that aim to maintain high-resolution feature maps during self-attention, our proposed LRSA computes self-attention in a low-resolution space, significantly reducing computational costs. Before delving into our proposed LRSA, let us first revisit the vision transformer architecture.

Revisiting self-attention in transformers. The vision transformer [15] has been demonstrated to be very powerful for computer vision [10], [17]–[20], [23]–[26]. It consists of two main parts: the multi-head self-attention (MHSA) and the feed-forward network (FFN). We continue by elaborating on MHSA. Given the input feature F_{in}, the query Q, key K

and value V are obtained with a linear transformation from F_{in}. Then, we can calculate the vanilla MHSA as

$$\text{Attention}(F_{in}) = \text{Softmax}(\frac{QK^T}{\sqrt{d_k}})V, \quad (1)$$

where d_k is the number of channels of F_{in}. We omit the multi-head operation for simplicity. The overall computational cost of vanilla self-attention is $O(N^2C + NC^2)$, where N and C are the number of tokens and the number of channels of $F_{in} \in \mathbb{R}^{N \times C}$, respectively. As the number of tokens of natural images are usually very large, the computational cost of vanilla self-attention is very high.

Previous solutions. To alleviate the computational cost while keeping the high-resolution of feature maps, recent downsampling-based vision transformers [9], [19], [20], [23], [26] change the self-attention computation to

$$\text{Attention}(F_{in}) = \text{Softmax}(\frac{QK_s^T}{\sqrt{d_k}})V_s, \quad (2)$$

in which K_s and V_s are the downsampled key K and value V with a fixed downsampling ratio s_r, respectively. The $1D \leftrightarrow 2D$ feature reshaping is omitted for convenience. The length of K_s and V_s is $1/s_r^2$ of the original K and V. If the original length of K and V is too large, the K_s and V_s will also be long sequences, introducing considerable computational cost in self-attention. Here, we only introduce downsampling-based transformers because they are most relevant to our method.

Our solution. Instead, we tackle the heavy computation of vanilla self-attention from a new perspective: we do not keep the high-resolution of feature maps but process the features in a very low-resolution space (Fig. 3 (b)). Specifically, the proposed LRSA downsamples the input feature F_{in} to a fixed size m. Then, multi-head self-attention is applied:

$$\text{Attention}(F_{in}) = \text{Softmax}(\frac{Q_pK_p^T}{\sqrt{d_k}})V_p, \quad (3)$$

where Q_p, K_p and V_p are obtained by a linear transformation from the downsampled F_{in}. Q_p, K_p and V_p are with a fixed size m, regardless of the resolution of the input F_{in}. Compared with vanilla self-attention and previous solutions, our LRSA has a much lower computational cost. LRSA can also facilitate attention optimization due to the much shorter token length. To fit the size of the original F_{in}, we then perform a bilinear interpolation after the self-attention calculation.

Complexity and characteristics. The computational complexity of LRSA is much lower than existing self-attention mechanisms for vision transformers. We summarize the main characteristics and computational complexity of recent popular self-attention mechanisms and our LRSA in Tab. 1. Spatial correlation means that self-attention is carried out in the spatial dimension, and some factorized transformers [73] compute self-attention in the channel dimension for reducing complexity. As can be observed from Tab. 1, other methods often face trade-offs among complexity, global receptive field, and spatial correlation. In contrast, our LRSA offers advantages in all these aspects.

Let us continue by analyzing the computational complexity of LRSA. For convenience, we do not include the 1D↔2D feature reshaping. LRSA first downsamples the input features $F_{in} \in \mathbb{R}^{N \times C}$ to a fixed size $m \times C$ with a 2D pooling operation, whose computational cost is $O(NC)$. Then, LRSA performs linear transformations and self-attention on the pooled features, which costs $O(mC^2)$. The computation of self-attention costs $O(m^2C)$. The final upsampling operation has the same computational cost as downsampling. Overall, the computational complexity of LRSA is $O(NC + mC^2 + m^2C)$. As m is a constant number (*e.g.*, 16^2) regardless of the value of N, we can simplify the complexity of LRSA to $O(NC + C^2)$, which is much smaller than existing methods.

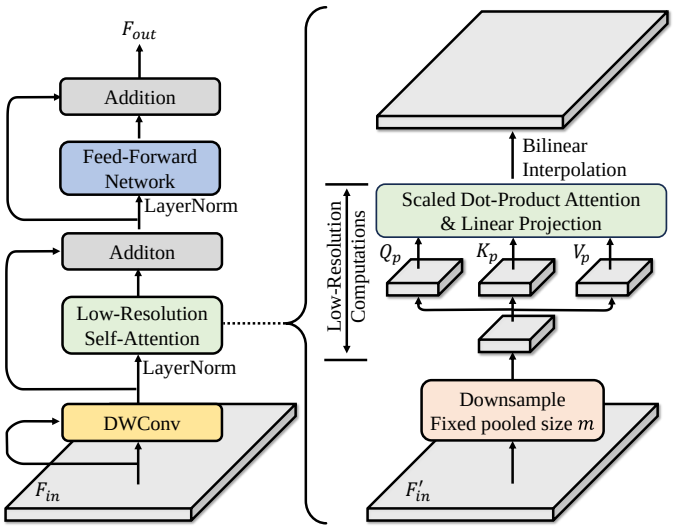

(a) Basic Block of LRFormer (b) Low-Resolution Self-Attention

Fig. 3. **Illustration of a basic block of our LRFormer.** We add a 3×3 depth-wise convolution (DWConv) with a residual connection before LRSA, which is also applied between the two linear layers of the FFN.

3.2 Low-Resolution Transformer

In this part, we build the LRFormer for semantic segmentation by incorporating the proposed LRSA. The overall architecture of LRFormer is illustrated in Fig. 4, with an encoder-decoder architecture.

Encoder-decoder. Taking a natural image as input, the encoder first downsamples it by a factor of 1/4, following prevailing literature in this field [17], [19], [20], [23], [26]. The encoder consists of four stages with a pyramid structure, each comprising multiple stacked basic blocks. In between every two stages, we include a patch embedding operation to reduce the feature size by half. This results in the extraction of multi-level features F_1, F_2, F_3, F_4 with strides of 4, 8, 16, and 32, respectively. We resize F_2, F_3, F_4 to the same size as F_2 before concatenating and squeezing them to smaller channels. The resulting features are then fed into our decoder head, which performs further semantic reasoning and outputs the final segmentation map via a 1×1 convolution layer. The details of our decoder head are presented in §3.3.

Basic block. The basic block is illustrated in Fig. 3. Like previous transformer blocks [17], [19], the basic block of our LRFormer is composed of a self-attention module and an FFN. The FFN is generally an MLP layer composed of

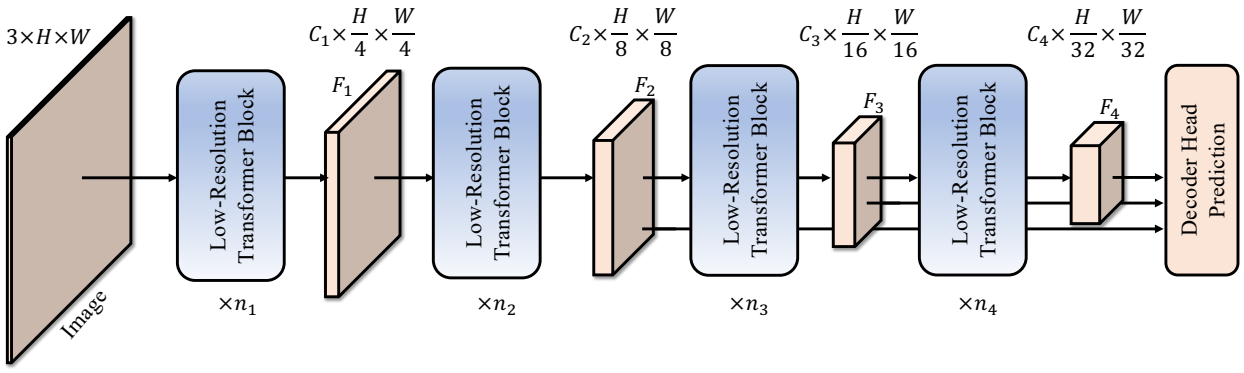

Fig. 4. **Pipeline of the proposed LRFormer.** F_2, F_3 and F_4 are fed into the decoder head for semantic segmentation.

two linear layers with GELU [74] activation in between. Differently, we renovate the self-attention module with our proposed LRSA. As LRSA is computed in a very low-resolution space, attaining a low complexity regardless of the input resolution. However, the low-resolution space may lose the spatial locality of the input features. Inspired by recent works [9], [20], [67], we further introduce depth-wise convolution (DWConv) in both positional encoding and FFN, assisting the feature extraction via capturing spatial local details. That is, we insert a 3×3 DWConv layer with short connection followed by our LRSA, providing conditional positional encoding [67]. This strategy is also applied between the two linear layers of the FFN. Therefore, our basic block can be simply formulated as below:

$$\begin{aligned} F'_{in} &= F_{in} + \text{DWConv}(F_{in}), \\ F_{att} &= F'_{in} + \text{LRSA}(\text{LayerNorm}(F'_{in})), \\ F_{out} &= F_{att} + \text{FFN}(\text{LayerNorm}(F_{att})), \end{aligned} \tag{4}$$

where F_{in}, F_{att} and F_{out} represent the input, output of LRSA, and output of the basic block, respectively. Since the complexity of DWCons is $O(NC)$, inserting DWConvs will still keep the overall self-attention complexity at $O(NC + C^2)$.

Architecture setting. To fit the budgets of different computational resources, we design four variants of LRFormer, namely LRFormer-T/S/B/L, stacking different numbers of basic blocks for each stage in the encoder. We summarize the detailed settings of their encoders in Tab. 2. In terms of ImageNet pretraining [75], the computational cost of LRFormer-T/S/B/L is similar to ResNet-18 [6] and Swin-T/S/B [17], respectively.

3.3 Decoder Head

In semantic segmentation, it is suboptimal to predict the results based solely on the final output of the encoder, as multi-level information is useful in perceiving objects with various scales and aspect ratios [9], [76]. Thus, we design a simple decoder for LRFormer to aggregate multi-level features efficiently and effectively. To this end, we note that an MLP aggregation can achieve good performance in the state-of-the-art work SegFormer [9]. However, it does not consider the spatial correlation between the features from different levels. Therefore, we encapsulate our LRSA into our decoder for feature refinement, strengthening the semantic reasoning of LRFormer.

As mentioned above, F_2, F_3, F_4 are resized to the same size as F_2 and then concatenated together. We apply a 1×1 convolution on the concatenated feature to squeeze the number of channels. Then, a basic block (LRSA + FFN) is adopted to refine the squeezed feature. As we know, the feature from the top of the encoder, *i.e.*, F_4, could be the most semantic meaningful. To avoid the loss of semantic information in the aggregation of high-level (F_4) and low-level (F_2, F_3) features, we concatenate the refined feature with F_4 to enhance the semantics. After that, another basic block is connected for further feature refinement. Finally, we infer the segmentation prediction from the refined feature with a simple 1×1 convolution. The experiments demonstrate that our simple decoder with LRSA can do better than previous state-of-the-art decoder heads for semantic segmentation, as shown in Tab. 10.

3.4 Implementation Details

In LRFormer, we apply the overlapped patch embedding, *i.e.*, a 3×3 convolution with a stride of 2, to downsample the features by half between each stage. To strengthen multi-scale learning of LRSA with negligible cost, we use pyramid pooling [20] to extract multi-scale features when computing the key and value features in LRSA. The desired fixed downsampling size m for generating the query, key and value is 16^2 for semantic segmentation. Such size is changed to 7^2 for ImageNet pretraining because $m = 16^2$ is too large for image classification. For the number of channels in the decoder, we set it to 256/384/512/640 for LRFormer-T/S/B/L, respectively.

4 Experiments

4.1 Experimental Setup

Datasets. We perform experiments on three well-established datasets. ADE20K [27] is a very challenging scene parsing dataset that contains 150 semantic classes with diverse foreground and background, consisting of 20K, 2K, and 3.3K images for training, validation, and testing, respectively. COCO-Stuff [28] labels both things and stuffs with a total of 171 fine-grained semantic labels, with 164K, 5K, 20K, and 20K images for training, validation, test-dev,

TABLE 2
Detailed settings of the encoders for different LRFormer variants, *i.e.*, T/S/B/L/XL. C, C_h, E, and n_i denote the number of feature channels, channels of each attention head, expansion ratio of FFN, and the number of basic blocks for the i-th stage, respectively.

Stage	Output Size	LRFormer-T	LRFormer-S	LRFormer-B	LRFormer-L	LRFormer-XL
1	$F_1 : \frac{H}{4} \times \frac{W}{4}$	$C = 48, E = 8$ $C_h = 24, n_1 = 2$	$C = 64, E = 8$ $C_h = 32, n_1 = 3$	$C = 80, E = 8$ $C_h = 40, n_1 = 4$	$C = 96, E = 8$ $C_h = 48, n_1 = 4$	$C = 128, E = 8$ $C_h = 64, n_1 = 4$
2	$F_2 : \frac{H}{8} \times \frac{W}{8}$	$C = 96, E = 8$ $C_h = 24, n_2 = 2$	$C = 128, E = 8$ $C_h = 32, n_2 = 3$	$C = 160, E = 8$ $C_h = 40, n_2 = 4$	$C = 192, E = 8$ $C_h = 48, n_2 = 6$	$C = 256, E = 8$ $C_h = 64, n_1 = 8$
3	$F_3 : \frac{H}{16} \times \frac{W}{16}$	$C = 240, E = 4$ $C_h = 24, n_3 = 6$	$C = 320, E = 4$ $C_h = 32, n_3 = 12$	$C = 400, E = 4$ $C_h = 40, n_3 = 15$	$C = 480, E = 4$ $C_h = 48, n_3 = 18$	$C = 640, E = 4$ $C_h = 64, n_3 = 22$
4	$F_4 : \frac{H}{32} \times \frac{W}{32}$	$C = 384, E = 4$ $C_h = 24, n_4 = 3$	$C = 512, E = 4$ $C_h = 32, n_4 = 3$	$C = 512, E = 4$ $C_h = 32, n_4 = 8$	$C = 640, E = 4$ $C_h = 40, n_4 = 8$	$C = 768, E = 4$ $C_h = 48, n_4 = 8$

and test challenge. Cityscapes [29] is a high-quality dataset for street scene parsing that contains 3K, 0.5K, and 1.5K driving images for training, validation, and testing. These datasets cover a wide range of semantic categories and pose different challenges for semantic segmentation models.

ImageNet pretraining. We adopt the popular *timm* package to implement our network. Following other networks, we first pretrain the backbone encoder of LRFormer on the ImageNet-1K dataset, which has 1.3M training and 50K validation images with 1K object categories. During ImageNet pretraining, the decoder head of LRFormer is omitted. To regularize the training process, we follow the standard data augmentation techniques and optimization strategy used in previous works [9], [17], [64]. We use AdamW [77] as the default optimizer with a learning rate of 0.001, weight decay of 0.05, a *cosine* learning rate adjustment schedule, and a batch size of 1024. No model EMA is applied. The backbone encoder is pretrained for 300 epochs, and we apply layer scale [78] to alleviate the overfitting of large networks, as suggested by recent works [59], [78]. For LRFormer-L, we follow [17], [59] additionally pretrain the network on the full ImageNet-22K dataset for 90 epochs and then finetune it on ImageNet-1K dataset for 30 epochs. In the finetuning, the learning rate is set as 5e-5, and each mini-batch has 512 images.

Training for semantic segmentation. We use *mmsegmentation* framework to train our network for semantic segmentation. AdamW [77] is adopted as the default optimizer, with learning of 0.00006, weight decay of 0.01, and *poly* learning rate schedule with factor 1.0. Following [9], [17], the weight decay of LayerNorm [84] layers is set as 0. Regarding the data augmentation, we use the same strategy as mentioned in [9], [17]. That is we construct the pipeline of image resizing ($0.5 \sim 2\times$), random horizontal flipping, followed by a random cropping of size 512×512, 512×512, and 1024×1024 for ADE20K, COCO-Stuff, and Cityscapes datasets, respectively. Note that for our largest model LRFormer-L in ADE20K, the cropped size remains 640×640, consistent with recent works. The mini-batch size is set to 16, 16, and 8 images for ADE20K, COCO-Stuff, and Cityscapes datasets, respectively. We train our network for 160K, 80K, and 160K iterations for ADE20K, COCO-Stuff, and Cityscapes datasets, respectively. We only use the cross-entropy loss for training and do not employ any extra losses like the auxiliary loss [4] and OHEM [85].

Testing for semantic segmentation. During testing, we maintain the original aspect ratio of the input image and resize it to a shorter size of 512 and a longer size not exceeding 2048 for the ADE20K and COCO-Stuff datasets. We follow the suggestion of [9] and resize the input size of LRFormer-L for the ADE20K dataset to a shorter size of 640 and a longer size not exceeding 2560. In the Cityscapes dataset, we apply a crop size of 1024×1024 with sliding window testing strategy following [9].

TABLE 3
Comparisons with recent methods on the ADE20K dataset [27]. The results of our method are marked as **bold**. "†" indicates the result pretrained on ImageNet-22K.

Method	FLOPs ↓	#Params ↓	mIoU ↑
SegFormer-B1 [9]	16G	14M	42.2%
Vim-Ti [79]	-	13M	41.0%
HRFormer-S [10]	109G	14M	44.0%
LRFormer-T (Ours)	17G	13M	**46.7%**
SegFormer-B2 [9]	62G	28M	46.5%
P2T-Small [20]	43G	28M	46.7%
MaskFormer [41]	55G	42M	46.7%
FeedFormer-B2 [47]	43G	29M	48.0%
Mask2Former [76]	74G	47M	47.7%
LRFormer-S (Ours)	40G	32M	**50.0%**
HRFormer-B [10]	280G	56M	48.7%
Vim-S [79]	-	46M	44.9%
SegFormer-B3 [9]	96G	47M	49.4%
LRFormer-B (Ours)	75G	69M	**51.0%**
DPT-Hybrid [80]	308G	124M	49.0%
SegFormer-B5 [9]	183G	85M	51.0%
DAViT-B [81]	294G	121M	49.4%
FasterViT-4 [82]	323G	457M	49.1%
InternImage-B [83]	296G	128M	50.8%
MaskFormer [41]	195G	102M	51.3%
LRFormer-L (Ours)	183G	113M	**52.6%**
SETR-MLA† [46]	-	302M	48.6%
MaskFormer† [76]	195G	102M	53.1%
CSWin-B† [18]	463G	109M	51.8%
LRFormer-L† (Ours)	183G	113M	**54.2%**

4.2 Comparisons

ADE20K. Results are shown in Tab. 3. LRFormer is compared with several recent transformer-based and Mamba-based methods in different complexity levels. Results of other methods are from their official repositories. We can observe that our LRFormer exhibits strong superiority over other

TABLE 4
Comparisons with recent transformer-based methods on the full COCO-Stuff dataset [28]. Results of our method are marked as **bold**.

Method	FLOPs ↓	#Params ↓	mIoU ↑
HRFormer-S [10]	109G	14M	37.9%
SegFormer-B1 [9]	16G	14M	40.2%
LRFormer-T (Ours)	17G	13M	**43.9%**
SegFormer-B2 [9]	62G	28M	44.6%
LRFormer-S (Ours)	40G	32M	**46.4%**
HRFormer-B [10]	280G	56M	42.4%
SegFormer-B3 [9]	79G	47M	45.5%
SegFormer-B5 [9]	112G	85M	46.7%
LRFormer-B (Ours)	75G	69M	**47.2%**
LRFormer-L (Ours)	122G	113M	**47.9%**

TABLE 5
Comparisons with recent transformer-based methods on the Cityscapes dataset [29]. Results of our method are marked as **bold**. FLOPs are calculated for an input size of 1024×2048.

Method	FLOPs ↓	#Params ↓	mIoU ↑
HRFormer-S [10]	872G	14M	80.0%
SegFormer-B1 [9]	244G	14M	78.5%
LRFormer-T (Ours)	122G	13M	**80.7%**
SegFormer-B2 [9]	717G	28M	81.0%
LRFormer-S (Ours)	295G	32M	**81.9%**
HRFormer-B [10]	2240G	56M	81.9%
SegFormer-B3 [9]	963G	47M	81.7%
SegFormer-B5 [9]	1460G	85M	82.4%
LRFormer-B (Ours)	555G	67M	**83.0%**
LRFormer-L (Ours)	908G	111M	**83.2%**

methods. In terms of the mIoU, LRFormer-T/S/B/L are 4.5%/3.5%/2.6%/1.6% better than SegFormer-B1/B2/B4/B5 [9], [17]. LRFormer-T is 2.3% better than Swin-T-based Mask2Former [76] with near half FLOPs. With ImageNet-22K pretraining, LRFormer is 1.1% and 2.4% better than the strongest Swin-B-based MaskFormer [17], [41] and UperNet-based CSwin [18], [86] with fewer FLOPs. Compared with the representative Mamba-based Vim [79] with linear complexity, our LRFormer is significantly better. The visualized Fig. 2 of accuracy-FLOPs shows a more intuitive view of the comparisons.

COCO-Stuff. We elaborate the results in Tab. 4. We evaluated our method on different network scales and compared it against recent popular methods. LRFormer achieved the highest mIoU on all network scales, outperforming the other methods. Specifically, our LRFormer-T model achieved a mIoU of 43.9%, which is 3.7% higher than HRFormer-S and 3.7% higher than SegFormer-B1. Similarly, our LRFormer-S and LRFormer-B models outperformed the corresponding SegFormer models by 1.8% and 1.7%. Our LRFormer-L model outperforms SegFormer-B5 by 1.2%. These experimental comparisons demonstrate the superiority of LRFormer on the COCO-Stuff dataset.

Cityscapes. Tab. 5 presents the experimental comparisons between LRFormer and recent popular methods on the Cityscapes dataset. LRFormer outperforms SegFormer and HRFormer in all cases. We can observe that due to large input size, FLOPs of other methods are much higher than ours.

TABLE 6
Classification results on ImageNet-1K [75] dataset. Results of our method are marked as **bold**. Results marked with "†" are pretrained on ImageNet-22K dataset.

Model	FLOPs ↓	#Params ↓	Size	Top-1 Acc. ↑
PVTv2-B1 [23]	2.1G	13M	224^2	78.7%
HAT-Net-T [71]	2.0G	13M	224^2	79.8%
P2T-Tiny [20]	1.8G	12M	224^2	79.8%
LRFormer-T (Ours)	1.8G	13M	224^2	**80.8%**
Swin-T [17]	4.5G	28M	224^2	81.5%
MViTv2-T [87]	4.7G	24M	224^2	82.3%
Vim-S [79]	-	26M	224^2	81.4%
HAT-Net-S [71]	4.3G	26M	224^2	82.6%
ConvNeXt-T [59]	4.5G	29M	224^2	82.1%
LRFormer-S (Ours)	4.7G	30M	224^2	**83.5%**
Swin-S [17]	8.7G	50M	224^2	83.0%
ConvNeXt-S [59]	8.7G	50M	224^2	83.1%
DAT-S [70]	9.0G	50M	224^2	83.7%
P2T-Large [20]	9.8G	55M	224^2	83.9%
LRFormer-B (Ours)	9.3G	62M	224^2	**84.5%**
DeiT-B [16]	17.5G	86M	224^2	81.8%
RegNetY-16G [88]	16.0G	84M	224^2	82.9%
RepLKNet-31B [60]	15.3G	79M	224^2	83.5%
SwinT-B [17]	15.4G	88M	224^2	83.5%
ConvNeXt-B [59]	15.4G	89M	224^2	83.8%
FocalNet-B [89]	15.4G	89M	224^2	83.9%
CSwin-B [18]	15.0G	78M	224^2	84.2%
DAT-B [70]	15.8G	88M	224^2	84.0%
Vim-B [79]	-	98M	224^2	83.2%
LRFormer-L (Ours)	15.7G	101M	224^2	**85.0%**
Swin-B† [17]	15.4G	88M	224^2	85.2%
ConvNeXt-B† [59]	15.4G	89M	224^2	85.8%
LRFormer-L† (Ours)	15.7G	101M	224^2	**86.4%**
ConvNeXt-B† [59]	45.1G	89M	384^2	86.8%
Swin-B† [17]	47.0G	88M	384^2	86.4%
LRFormer-L† (Ours)	46.3G	101M	384^2	**87.2%**
Swin-L† [17]	34.5G	197M	224^2	86.3%
ConvNeXt-L† [59]	34.4G	198M	224^2	86.6%
LRFormer-XL† (Ours)	31.6G	187M	224^2	**87.0%**

For example, SegFormer-B2 costs 717G FLOPs while our LRFormer-S only spends 41% FLOPs with 0.9% improvement. More complexity analysis can refer to Tab. 12.

ImageNet. Since we pretrained our backbone encoder on ImageNet, we also evaluate our network on ImageNet classification only for reference. Results are shown in Tab. 6. We divide them to five groups. The four groups are divided by the FLOPs of approximate 2G, 4.5G, 9G, 16G, respectively. The fifth and sixth groups include results pretrained on ImageNet-22K dataset. The backbone encoder of our LRFormer outperformed recent state-of-the-art CNN-based methods such as ConvNeXt [59] and RepLKNet [60], and transformer-based methods like DAT [70] and P2T [20].

4.3 Visualization analysis.

To visually illustrate the effectiveness of our method, we pick segformer [9] as the model for intuitive comparison from ADE20K val set and Cityscapes val set, as shown in Fig. 5 and Fig. 6 respectively. The results indicate that LRFormer is capable of generating more precise segmentation maps, particularly in the areas highlighted by the red boxes. We

TABLE 7
Experiments on the fixed pooled size settings of our LRSA. The performance is saturated when pooled size is larger than 16×16.

Pooled Size ↓	FLOPs ↓	Training Memory ↓	mIoU ↑
4×4	38G (-5%)	3.9GB (-7%)	46.3%
8×8	38G (-5%)	4.0GB (-5%)	46.8%
16×16	40G	4.2GB	48.5%
32×32	52G (+30%)	5.3GB (+26%)	48.6%
48×48	74G (+85%)	7.4GB (+76%)	48.7%
64×64	108G (+170%)	10.9GB (+160%)	48.5%

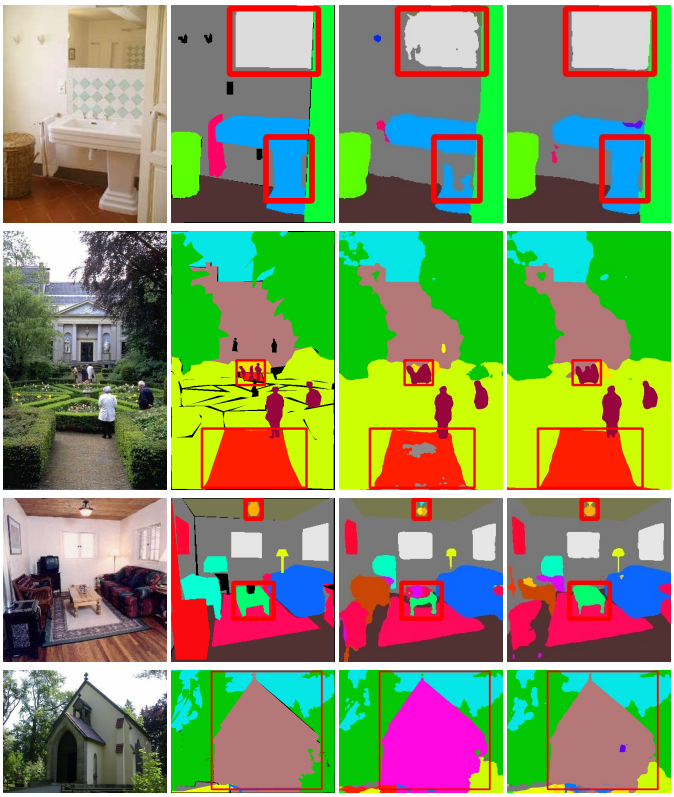

Fig. 5. **Qualitative Visualization on ADE20K val set.** The figures from left to right are input images, ground truth, segmentation maps of SegFormer [9], segmentation maps of our LRFormer. Significant improvements are indicated by red boxes on segmentation maps.

discover that LRFormer offers significant advantages in terms of maintaining object segmentation integrity and capturing intricate details.

4.4 Ablation Study

In the following part, we conduct several ablation studies to analyze our LRFormer. Except for specifically mentioning, we use the following settings. LRFormer-S is set as the baseline and trained using 8 GPUs for both classification and semantic segmentation. For classification, our network is trained for 100 epochs in the ImageNet-1K [75] dataset. For semantic segmentation, our network is trained for 80K iterations in the ADE20K [27] dataset. Other settings are kept same as the setup in §4.1.

Fixed pooled size. We reported the results in Tab. 7 for ADE20K semantic segmentation. For each basic block, the pooling operation will be omitted if the feature map size is smaller than the desired pooled size. Default fixed pooled size m is 16^2 for semantic segmentation. Results show larger pooled size ($m \geq 16^2$) achieves saturated performance. The default setting only introduces 5% training memory overhead and FLOPs compared with the pooled size of 8^2 for semantic segmentation. Further decreasing the pooled size to 4^2 will not introduce significant gain on improving efficiency. When increasing the pooled size to $32^2, 48^2, 64^2$, we obtain a minor improvement or even decreased performance on ADE20K semantic segmentation. We also observe that the FLOPs and training memory overhead are much more significant (26% $\sim$ 170%) when the pooled size is larger than 16^2. We then conduct similar experiments on Cityscapes dataset, which has a much larger input size (1024×1024). The mIoU results of LRFormer-L for pooled size of 16^2 and 32^2 are both 83.2%, showing that the default pooled size can also work well on larger input size. While adjusting pooled size based on input resolution could preserve more detail for small objects, our fixed-size design works well across all object scales. The high-resolution DWConv branch and multi-level feature aggregation effectively maintain small object information despite the spatial reduction. Furthermore, ideal backbone design paradigms [6], [17], [19], [59] suggest basic blocks maintaining consistent settings (same pooled size in our network) across different stages. This architectural simplicity enhances implementation efficiency and reduces the effort of finding optimal parameters for each stage individually. Considering the performance, FLOPs, training memory, and ideal backbone design paradigm, we use fixed low-resolution pooled size as the default setting.

TABLE 8
Performance comparison between the 16×16 pooled size (original) and smaller pooled size (4×4).

Category	Metric	Default	Smaller	Relative Change
Small	mIoU	36.2%	33.7%	-7.1%
	mAcc	46.3%	42.3%	-8.8%
Medium	mIoU	48.1%	45.3%	-5.7%
	mAcc	59.7%	56.8%	-4.9%
Large	mIoU	57.2%	53.8%	-6.0%
	mAcc	68.3%	64.3%	-5.9%

Locality capturing. Our LRSA only computes the attention in low-resolution space. Introducing spatial locality, 3×3 depth-wise convolution, to our network is beneficial for getting fine-grained semantic maps. In Tab. 9, we analyzed the effect of the two depth-wise convolution before LRSA and in FFN. The number of GFLOPs for these three configurations is very similar so it is not reported. We can observe that the ADE20K performance of our LRFormer is improved by 0.5% and 1.4% and when adding the depth-wise convolution before LRSA in FFN, with 5% and 24% training memory overhead. If both depth-wise convolutions are removed, the mIoU performance will further drop 2.4% with 0.7GB less training memory usage, compared with the results only without the depth-wise convolution in FFN. This indicates that locality capturing plays a significant role in LRFormer. Therefore, we add both of them in our LRFormer.

Performance on small objects. To investigate how pooled size affects different-sized objects, we categorize ADE20K semantic classes into small, medium, and large categories. Discrete objects were classified based on their typical real-

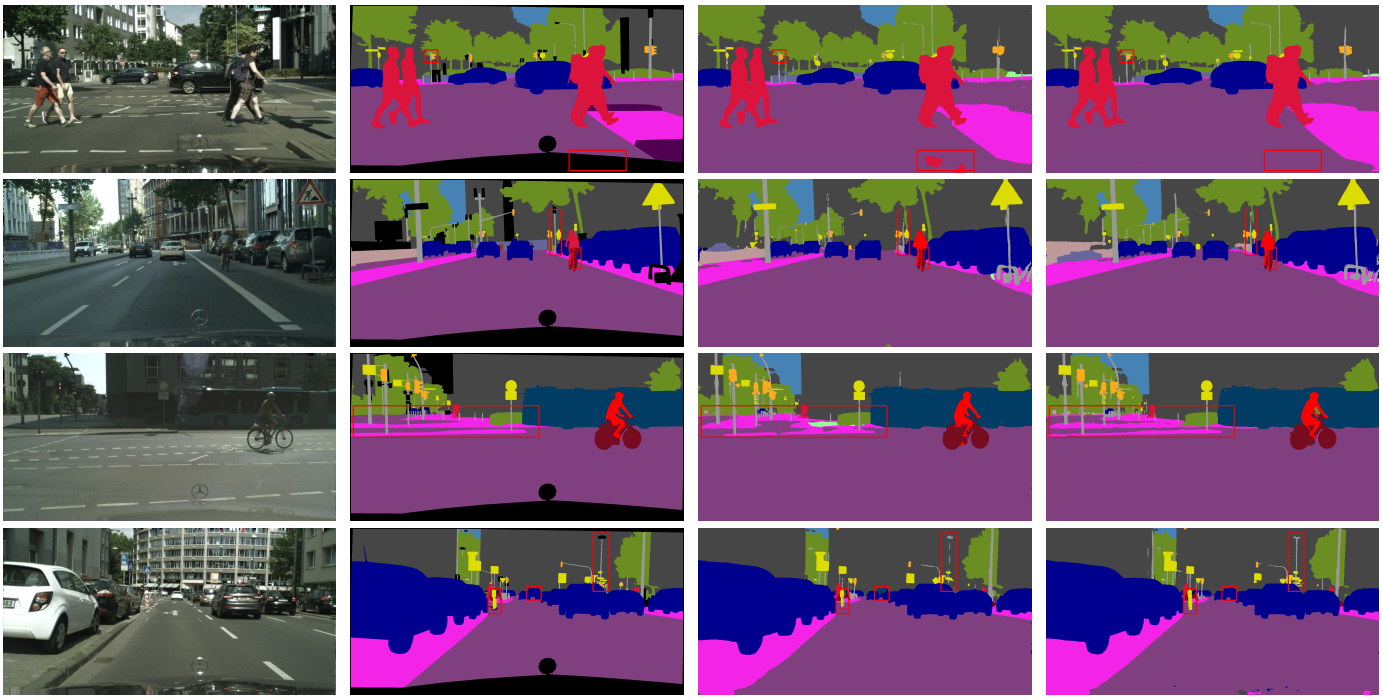

Fig. 6. **Qualitative Visualization on Cityscapes val set.** The figures from left to right are input images, ground truth, segmentation maps of SegFormer [9], segmentation maps of our LRFormer. The significant improvements are indicated by red boxes on segmentation maps.

TABLE 9
Ablation study on the spatial locality capturing. "Memory" is the training memory in ImageNet pretraining.

Method	Memory	Top-1 Acc. ↑	mIoU ↑
LRFormer-S	14.5GB	81.6%	48.5%
w/o DWConv (bef. LRSA)	13.8GB	81.4%	48.0%
w/o DWConv (FFN)	11.7GB	81.1%	47.1%
w/o DWConv (Both)	11.0GB	80.4%	44.7%

TABLE 10
Comparisons of our simple decoder and other popular decoder heads.

Decoder Head	FLOPs ↓	#Params ↓	mIoU ↑
Ours	40G	32M	49.5%
w/ OCR [21]	48G	34M	48.0%
w/ PPM [4]	82G	44M	48.4%
w/ DA [2]	94G	42M	48.9%
w/ CC [8]	84G	42M	48.6%

world dimensions, while amorphous regions (*e.g.*, sky) were included in the large category due to their typically extensive spatial coverage in images. Results are shown in Tab. 8. Using a smaller pooled size (4×4) instead of our default setting degrades performance across all categories, with small objects experiencing the most severe impact. This confirms that downsampling features to a resolution that is too small (*e.g.*, 4×4) can lose important semantics particularly for small objects.

Comparions of different decoder heads. Our decoder head aims to predict the semantic maps from multi-level feature maps effectively and efficiently with LRSA. The validate the LRSA of our decoder head, we compare it with several popular decode heads. These popular decoder heads are designed for CNNs, whose output feature maps are usually 1/8 of the original image. However, the backbone encoder of our LRFormer can output features of the 1/32 of the original image. To make a fair comparison, we first upsample features of the last stages and concatenate them together. Then, we feed them to the popular decoder heads. Other processes keep unchanged in these popular decoder heads. Tab. 10 summarized the results on ADE20K semantic segmentation. The backbone is pretrained for 300 epochs on ImageNet-1K. Compared with PPM [4], DA [2], and CC [8], our LRFormer achieves 1.1%, 0.6%, and 0.9% improvement, respectively, with only fewer than 50% FLOPs. Compared with OCR [21], our LRFormer obtains 1.5% performance gain, with 83% FLOPs. Therefore, our default setting is more efficient and effective than other popular decoder heads.

Bilinear interpolation. Although the self-attention is computed in a low-resolution manner, a bilinear interpolation is needed to fit the size as requested by the residual connection. However, we find that using LRFormer-S with an input size of 512^2, the bilinear interpolation only has a latency of 0.1ms, constituting a negligible 0.8% of the overall network's latency.

Decoder head with other backbones. In this part, we conduct an experiment on SegFormer-B2 replacing with our decoder. We find that SegFormer-B2 with our decoder achieves 47.3% mIoU, 0.8% better than the initial SegFormer-B2 with less 28 GFLOPs. Thus, replacing SegFormer-B2's decoder with ours can introduce a significant improvement in terms of the performance and efficiency.

Dimensions of the decoder head. To optimize the performance and computational cost of the decoder head, we employ a 1×1 convolution to reduce the dimension of

TABLE 11
Discussions on the dimensions of the decoder. When the dimension of the decoder is larger than 384, the performance will be saturated or even decreased.

Dimension	FLOPs ↓	#Params ↓	mIoU ↑
128	27G	30M	47.8%
256	32G	31M	49.2%
384	40G	32M	49.5%
512	50G	37M	49.6%
768	79G	46M	49.2%
1024	117G	58M	49.2%

TABLE 12
Analysis of the memory usage and FLOPs for different input size. "Att. FLOPs" indicates the summation of MHSA and upsampling operations. "Memory" is the training memory for semantic segmentation.

Method	Size, Batch Size	Memory ↓	FLOPs ↓	Att. FLOPs ↓
LRFormer-S	512×512, 2	4.2GB	40G	0.8G
SegFormer-B2	512×512, 2	7.2GB	62G	3.4G
LRFormer-S	1024×1024, 1	5.7GB	145G	0.9G
SegFormer-B2	1024×1024, 1	18.8GB	279G	54.0G
LRFormer-S	1536×1536, 1	15.3GB	319G	1.1G
SegFormer-B2	1536×1536, 1	OOM	802G	293.6G

TABLE 13
Comparisons with recent query-based frameworks on the ADE20K dataset [27]. The results of our method are marked as **bold**. Methods ended with "+" are the enhanced versions upgraded with Mask2Former's decoder. "†" indicates the result pretrained on ImageNet-22K and with a larger image size 640×640.

Method	FLOPs ↓	#Params ↓	mIoU ↑
Mask2Former (Swin-T [17])	74G	47M	47.7%
Mask2Former (Swin-S [17])	98G	69M	51.3%
P2T-T+ [20]	56G	31M	48.2%
P2T-S+ [20]	70G	43M	49.6%
P2T-B+ [20]	109G	74M	52.5%
LRFormer-T+ (Ours)	53G	31M	**49.4%**
LRFormer-S+ (Ours)	70G	48M	**51.3%**
LRFormer-B+ (Ours)	94G	80M	**53.7%**
MaskFormer (Swin-B [17])†	195G	102M	53.1%
Mask2Former (Swin-B [17])†	223G	107M	53.9%
Mask DINO (Swin-B [17])†	265G	110M	54.2%
SeMask (Swin-B [17])†	227G	110M	54.4%
LRFormer-L+† (Ours)	192G	119M	**55.8%**
MaskFormer (Swin-L [17])†	375G	212M	54.3%
Mask2Former (Swin-L [17])†	403G	215M	56.1%
Mask DINO (Swin-L [17])†	431G	223M	56.6%
SeMask (Swin-L [17])†	426G	223M	56.3%
LRFormer-XL+† (Ours)	365G	205M	**58.1%**

the concatenated multi-level features before feeding them into the decoder. We conducted experiments with various dimension settings and compared their results in Tab. 11. The backbone is pretrained for 300 epochs on ImageNet-1K. The experiments show that a dimension setting of 512 achieves the best performance. However, setting the dimension to 384 results in only a 0.1% drop in mIoU performance, while saving 25% FLOPs. Therefore, we set the dimension of the decoder head to 384 in our LRFormer-S, reflecting the optimal trade-off between performance and computational cost.

Memory and FLOPs. Our LRSA has a very low computational complexity of only $O(C^2 + CN)$. We numerically analyze the efficiency of our LRFormer for different input sizes, as well as the comparisons with the representative method SegFormer [9]. The analyzed results on FLOPs, attention FLOPs, and training memory are shown in Tab. 12. For LRFormer, we additionally include the computational cost of upsampling operations. Our LRFormer-S costs much less memory and FLOPs than SegFormer-B2. Given input size of 1024×1024, the number of FLOPs of MHSA operations in our LRFormer is dramatically lower than (0.9G *vs.* 54G) the self-attention in SegFormer. We can also observe that when the input size is increasingly larger, the superiority of LRFormer will be more substantial. This is because increasing input size will only slightly increase the FLOPs of upsampling operations in our MHSA.

4.5 Advanced LRFormer with Query-based Decoders

Recently, there emerged some query-based frameworks like MaskFormer series [41], [42]. Though the decoders of them are a bit more complex than direct fusion strategy like SegFormer, they can achieve outstanding performance with transformers for semantic segmentation. As mentioned before, LRFormer uses a direct fusion strategy following previous works, showing that a simple decoding strategy can also achieve state-of-the-art performance. In this part, we would like to explore the potential of LRFormer combined with query-based decoders. We build a stronger version LRFormer+, which is the LRFormer encoder paired with the Mask2Former decoder. We make a comparison with recent methods that applied query-based decoders, *i.e.*, Mask2Former [42], Mask DINO [45], and SeMask [90]. Since Mask DINO and SeMask only have an implementation based on larger backbone like Swin-L, for a fair comparison, we reimplement these two methods with Swin-B backbone using their official code. We also build a powerful method P2T+ with the recent powerful P2T [20] upgraded with the decoder of Mask2Former for a more comprehensive analysis.

We conduct the experiments in the ADE20K dataset, following the same experimental setup. Results are shown in Tab. 13. LRFormer+ demonstrated superior performance outshining recent query-based frameworks such as Mask2Former and Mask DINO. We can observe that Mask DINO† is 0.2% better than Mask2Former† with additional 42G FLOPs. SeMask† is a more efficient architecture, which surpasses Mask2Former† by 0.5% with 4G more FLOPs. When comparing the upgraded LRFormer+ with a Mask2Former model utilizing the Swin-B backbone, LRFormer+ achieved 1.9% higher mIoU than Mask2Former, despite LRFormer+ having slightly more parameters but significantly 31G lower FLOPs, indicating a more efficient architecture. Furthermore, the implementation of Mask2Former with the innovative P2T backbone showcased enhanced capabilities, with the P2T-L variant reaching a mIoU of 52.5%, 1.2% better than Swin-S version of Mask2Former with similar FLOPs. Nonetheless, LRFormer+ still outperformed this configuration. For example, LRFormer-B+ is 1.2% further better than the enhanced P2T-L+ version.

For a more intuitive analysis, we visualized the accuracy-FLOPs comparisons of Tab. 3 and Tab. 13 in Fig. 2. From the curve and the data points of this figure, LRFormer series achieve higher accuracy with fewer FLOPs compared to all

TABLE 14
Performance comparison of different backbones on the vision-language model LISA [91] for referring segmentation.

Backbone	gIoU (%)	cIoU (%)
ViT-L [15]	36.9	41.1
Swin-L [17]	38.1	43.1
LRFormer-XL (Ours)	**40.9**	**45.7**

other models, like Mask2Former [42], Mask DINO [45], and P2T [20].

4.6 Application to Vision-Language Models

While semantic segmentation remains fundamental in computer vision, the community has also shown growing interest in reasoning segmentation tasks. These new tasks integrate visual perception with language understanding capabilities [91]–[94]. These tasks, exemplified by representative works like LISA [91], leverage large vision-language models such as CLIP [92] and LLaVA [93] to segment objects based on textual descriptions. To demonstrate the versatility of our proposed LRFormer beyond semantic segmentation, we conduct experiments on referring segmentation to verify whether our backbone can enhance the performance of vision-language models.

Experimental setup. For our evaluation, we use LISA [91] with LLaVA-7B-v1 [93] as the baseline. We only replace the vision backbone of LISA [91] with three different options: ViT-L [15], Swin-L [17], and our LRFormer-XL, while keeping all other components consistent. Each backbone is pretrained on the COCO dataset [95] to ensure a fair comparison, and we maintain the same architecture for other parts of the vision branch. We use the official strategy [91] to train each method and test on the ReasonSeg validation set [91] for referring segmentation, which allows segmenting specific objects in images based on language prompts. Following previous works [91], [96], [97], we use gIoU and cIoU as evaluation metrics. More details of these metrics can refer to [91].

Results. Tab. 14 shows the performance comparison of different backbones. Our LRFormer-XL backbone significantly outperforms both ViT-L [15] and Swin-L [17] across both metrics. Specifically, LRFormer-XL achieves 40.9% gIoU and 45.7% cIoU, surpassing the ViT-L [15] backbone by 4.0% and 4.6% in gIoU and cIoU, and the Swin-L [17] backbone by 2.8% and 2.6%, respectively. These results validate that our LRFormer effectively captures global context while preserving fine-grained details necessary for reasoning tasks. The consistent performance improvements across both conventional semantic segmentation and referring segmentation highlight the versatility and potential of our architecture for various advanced vision-language applications.

5 Conclusion

In this paper, we presented a novel approach to semantic segmentation via introducing the low-resolution self-attention. LRSA computes the self-attention in a fixed low-resolution space, regardless of the size of the input image, making the self-attention highly efficient. Extensive experiments (*e.g.*, Fig. 2) on ADE20K [27], COCO-Stuff [28] and Cityscapes [29] datasets show that LRFormer outperforms state-of-the-art models, suggesting that LRSA is adequate to keep global receptive field with negligible computational cost, *i.e.*, FLOPs. This study provides evidence for the effectiveness of LRSA and opens a new direction for future research.

Acknowledgements. This work is funded by NSFC (No. 62225604, 62176130), the Fundamental Research Funds for the Central Universities (Nankai University, 070-63233089), and A*STAR Career Development Fund (No. C233312006), and National Research Foundation Singapore under its AI Singapore Programme (AISG Award No: AISG2-GC-2023-007). Computation was partially supported by the Supercomputing Center of Nankai University. The computational work for this article was partially performed on resources of the National Supercomputing Centre, Singapore (https://www.nscc.sg).

References

[1] L.-C. Chen, G. Papandreou, I. Kokkinos, K. Murphy, and A. L. Yuille, "Deeplab: Semantic image segmentation with deep convolutional nets, atrous convolution, and fully connected crfs," *IEEE Trans. Pattern Anal. Mach. Intell.*, vol. 40, no. 4, pp. 834–848, 2017.
[2] J. Fu, J. Liu, H. Tian, Y. Li, Y. Bao, Z. Fang, and H. Lu, "Dual attention network for scene segmentation," in *IEEE Conf. Comput. Vis. Pattern Recog.*, 2019, pp. 3146–3154.
[3] Z. Zhu, M. Xu, S. Bai, T. Huang, and X. Bai, "Asymmetric non-local neural networks for semantic segmentation," in *Int. Conf. Comput. Vis.*, 2019, pp. 593–602.
[4] H. Zhao, J. Shi, X. Qi, X. Wang, and J. Jia, "Pyramid scene parsing network," in *IEEE Conf. Comput. Vis. Pattern Recog.*, 2017, pp. 2881–2890.
[5] M. Yang, K. Yu, C. Zhang, Z. Li, and K. Yang, "DenseASPP for semantic segmentation in street scenes," in *IEEE Conf. Comput. Vis. Pattern Recog.*, 2018, pp. 3684–3692.
[6] K. He, X. Zhang, S. Ren, and J. Sun, "Deep residual learning for image recognition," in *IEEE Conf. Comput. Vis. Pattern Recog.*, 2016, pp. 770–778.
[7] S. Xie, R. Girshick, P. Dollár, Z. Tu, and K. He, "Aggregated residual transformations for deep neural networks," in *IEEE Conf. Comput. Vis. Pattern Recog.*, 2017, pp. 1492–1500.
[8] Z. Huang, X. Wang, Y. Wei, L. Huang, H. Shi, W. Liu, and T. S. Huang, "CCNet: Criss-cross attention for semantic segmentation," *IEEE Trans. Pattern Anal. Mach. Intell.*, vol. 45, no. 06, pp. 6896–6908, 2023.
[9] E. Xie, W. Wang, Z. Yu, A. Anandkumar, J. M. Alvarez, and P. Luo, "Segformer: Simple and efficient design for semantic segmentation with transformers," *Adv. Neural Inform. Process. Syst.*, vol. 34, pp. 12 077–12 090, 2021.
[10] Y. Yuan, R. Fu, L. Huang, W. Lin, C. Zhang, X. Chen, and J. Wang, "Hrformer: High-resolution vision transformer for dense predict," *Adv. Neural Inform. Process. Syst.*, vol. 34, pp. 7281–7293, 2021.
[11] H. Zhao, Y. Zhang, S. Liu, J. Shi, C. C. Loy, D. Lin, and J. Jia, "PSANet: Point-wise spatial attention network for scene parsing," in *Eur. Conf. Comput. Vis.*, 2018, pp. 267–283.
[12] H. Zhang, K. Dana, J. Shi, Z. Zhang, X. Wang, A. Tyagi, and A. Agrawal, "Context encoding for semantic segmentation," in *IEEE Conf. Comput. Vis. Pattern Recog.*, 2018, pp. 7151–7160.
[13] C. Yu, J. Wang, C. Peng, C. Gao, G. Yu, and N. Sang, "Learning a discriminative feature network for semantic segmentation," in *IEEE Conf. Comput. Vis. Pattern Recog.*, 2018, pp. 1857–1866.
[14] T. Takikawa, D. Acuna, V. Jampani, and S. Fidler, "Gated-scnn: Gated shape cnns for semantic segmentation," in *Int. Conf. Comput. Vis.*, 2019, pp. 5229–5238.
[15] A. Dosovitskiy, L. Beyer, A. Kolesnikov, D. Weissenborn, X. Zhai, T. Unterthiner, M. Dehghani, M. Minderer, G. Heigold, S. Gelly *et al.*, "An image is worth 16x16 words: Transformers for image recognition at scale," in *Int. Conf. Learn. Represent.*, 2021.
[16] H. Touvron, M. Cord, M. Douze, F. Massa, A. Sablayrolles, and H. Jégou, "Training data-efficient image transformers & distillation through attention," *arXiv preprint arXiv:2012.12877*, 2020.

[17] Z. Liu, Y. Lin, Y. Cao, H. Hu, Y. Wei, Z. Zhang, S. Lin, and B. Guo, "Swin transformer: Hierarchical vision transformer using shifted windows," in *Int. Conf. Comput. Vis.*, 2021, pp. 10 012–10 022.

[18] X. Dong, J. Bao, D. Chen, W. Zhang, N. Yu, L. Yuan, D. Chen, and B. Guo, "Cswin transformer: A general vision transformer backbone with cross-shaped windows," in *IEEE Conf. Comput. Vis. Pattern Recog.*, 2022, pp. 12 124–12 134.

[19] W. Wang, E. Xie, X. Li, D.-P. Fan, K. Song, D. Liang, T. Lu, P. Luo, and L. Shao, "Pyramid vision transformer: A versatile backbone for dense prediction without convolutions," in *Int. Conf. Comput. Vis.*, 2021, pp. 568–578.

[20] Y.-H. Wu, Y. Liu, X. Zhan, and M.-M. Cheng, "P2T: Pyramid pooling transformer for scene understanding," *IEEE Trans. Pattern Anal. Mach. Intell.*, vol. 45, no. 11, pp. 12 760–12 771, 2023.

[21] Y. Yuan, X. Chen, and J. Wang, "Object-contextual representations for semantic segmentation," in *Eur. Conf. Comput. Vis.* Springer, 2020, pp. 173–190.

[22] F. Yu and V. Koltun, "Multi-scale context aggregation by dilated convolutions," in *Int. Conf. Learn. Represent.*, 2016.

[23] W. Wang, E. Xie, X. Li, D.-P. Fan, K. Song, D. Liang, T. Lu, P. Luo, and L. Shao, "PVT v2: Improved baselines with pyramid vision transformer," *Computational Visual Media*, vol. 8, no. 3, pp. 415–424, 2022.

[24] Z. Liu, H. Hu, Y. Lin, Z. Yao, Z. Xie, Y. Wei, J. Ning, Y. Cao, Z. Zhang, L. Dong *et al.*, "Swin transformer v2: Scaling up capacity and resolution," in *IEEE Conf. Comput. Vis. Pattern Recog.*, 2022, pp. 12 009–12 019.

[25] J. Yang, C. Li, P. Zhang, X. Dai, B. Xiao, L. Yuan, and J. Gao, "Focal self-attention for local-global interactions in vision transformers," *arXiv preprint arXiv:2107.00641*, 2021.

[26] H. Fan, B. Xiong, K. Mangalam, Y. Li, Z. Yan, J. Malik, and C. Feichtenhofer, "Multiscale vision transformers," in *Int. Conf. Comput. Vis.*, 2021, pp. 6824–6835.

[27] B. Zhou, H. Zhao, X. Puig, S. Fidler, A. Barriuso, and A. Torralba, "Scene parsing through ade20k dataset," in *IEEE Conf. Comput. Vis. Pattern Recog.*, 2017, pp. 633–641.

[28] H. Caesar, J. Uijlings, and V. Ferrari, "COCO-Stuff: Thing and stuff classes in context," in *IEEE Conf. Comput. Vis. Pattern Recog.*, 2018, pp. 1209–1218.

[29] M. Cordts, M. Omran, S. Ramos, T. Rehfeld, M. Enzweiler, R. Benenson, U. Franke, S. Roth, and B. Schiele, "The cityscapes dataset for semantic urban scene understanding," in *IEEE Conf. Comput. Vis. Pattern Recog.*, 2016, pp. 3213–3223.

[30] J. Long, E. Shelhamer, and T. Darrell, "Fully convolutional networks for semantic segmentation," in *IEEE Conf. Comput. Vis. Pattern Recog.*, 2015, pp. 3431–3440.

[31] L.-C. Chen, G. Papandreou, F. Schroff, and H. Adam, "Rethinking atrous convolution for semantic image segmentation," *arXiv preprint arXiv:1706.05587*, 2017.

[32] H. Ding, X. Jiang, A. Q. Liu, N. M. Thalmann, and G. Wang, "Boundary-aware feature propagation for scene segmentation," in *Int. Conf. Comput. Vis.*, 2019, pp. 6819–6829.

[33] X. Li, X. Li, L. Zhang, G. Cheng, J. Shi, Z. Lin, S. Tan, and Y. Tong, "Improving semantic segmentation via decoupled body and edge supervision," in *Eur. Conf. Comput. Vis.* Springer, 2020, pp. 435–452.

[34] Y. Yuan, J. Xie, X. Chen, and J. Wang, "Segfix: Model-agnostic boundary refinement for segmentation," in *Eur. Conf. Comput. Vis.* Springer, 2020, pp. 489–506.

[35] M. Zhen, J. Wang, L. Zhou, S. Li, T. Shen, J. Shang, T. Fang, and L. Quan, "Joint semantic segmentation and boundary detection using iterative pyramid contexts," in *IEEE Conf. Comput. Vis. Pattern Recog.*, 2020, pp. 13 666–13 675.

[36] Y. Yuan, L. Huang, J. Guo, C. Zhang, X. Chen, and J. Wang, "Ocnet: Object context network for scene parsing," *arXiv preprint arXiv:1809.00916*, 2018.

[37] Y.-H. Wu, S.-H. Gao, J. Mei, J. Xu, D.-P. Fan, R.-G. Zhang, and M.-M. Cheng, "JCS: An explainable covid-19 diagnosis system by joint classification and segmentation," *IEEE Trans. Image Process.*, vol. 30, pp. 3113–3126, 2021.

[38] Y. Wang, Y. Li, J. H. Elder, R. Wu, and H. Lu, "Class-conditional domain adaptation for semantic segmentation," *Computational Visual Media*, vol. 10, no. 5, pp. 1013–1030, 2024.

[39] D. Liang, Y. Sun, Y. Du, S. Chen, and S.-J. Huang, "Relative difficulty distillation for semantic segmentation," *Science China Information Sciences*, vol. 67, no. 9, p. 192105, 2024.

[40] Z. Li, W. Wang, E. Xie, Z. Yu, A. Anandkumar, J. M. Alvarez, P. Luo, and T. Lu, "Panoptic segformer: Delving deeper into panoptic segmentation with transformers," in *IEEE Conf. Comput. Vis. Pattern Recog.*, 2022, pp. 1280–1289.

[41] B. Cheng, A. Schwing, and A. Kirillov, "Per-pixel classification is not all you need for semantic segmentation," *Adv. Neural Inform. Process. Syst.*, vol. 34, pp. 17 864–17 875, 2021.

[42] B. Cheng, I. Misra, A. G. Schwing, A. Kirillov, and R. Girdhar, "Masked-attention mask transformer for universal image segmentation," in *IEEE Conf. Comput. Vis. Pattern Recog.*, 2022, pp. 1290–1299.

[43] W. Zhang, J. Pang, K. Chen, and C. C. Loy, "K-net: Towards unified image segmentation," *Adv. Neural Inform. Process. Syst.*, vol. 34, pp. 10 326–10 338, 2021.

[44] Q. Yu, H. Wang, S. Qiao, M. Collins, Y. Zhu, H. Adam, A. Yuille, and L.-C. Chen, "K-means mask transformer," in *Eur. Conf. Comput. Vis.* Springer, 2022, pp. 288–307.

[45] F. Li, H. Zhang, H. Xu, S. Liu, L. Zhang, L. M. Ni, and H.-Y. Shum, "Mask DINO: Towards a unified transformer-based framework for object detection and segmentation," in *IEEE Conf. Comput. Vis. Pattern Recog.*, 2023, pp. 3041–3050.

[46] S. Zheng, J. Lu, H. Zhao, X. Zhu, Z. Luo, Y. Wang, Y. Fu, J. Feng, T. Xiang, P. H. Torr *et al.*, "Rethinking semantic segmentation from a sequence-to-sequence perspective with transformers," in *IEEE Conf. Comput. Vis. Pattern Recog.*, 2021, pp. 6881–6890.

[47] J.-h. Shim, H. Yu, K. Kong, and S.-J. Kang, "Feedformer: Revisiting transformer decoder for efficient semantic segmentation," in *AAAI Conf. Artif. Intell.*, vol. 37, no. 2, 2023, pp. 2263–2271.

[48] Y. Fang, W. Wang, B. Xie, Q. Sun, L. Wu, X. Wang, T. Huang, X. Wang, and Y. Cao, "EVA: Exploring the limits of masked visual representation learning at scale," in *IEEE Conf. Comput. Vis. Pattern Recog.*, 2023, pp. 19 358–19 369.

[49] J. Jain, J. Li, M. T. Chiu, A. Hassani, N. Orlov, and H. Shi, "Oneformer: One transformer to rule universal image segmentation," in *IEEE Conf. Comput. Vis. Pattern Recog.*, 2023, pp. 2989–2998.

[50] P. Wang, S. Wang, J. Lin, S. Bai, X. Zhou, J. Zhou, X. Wang, and C. Zhou, "ONE-PEACE: Exploring one general representation model toward unlimited modalities," *arXiv preprint arXiv:2305.11172*, 2023.

[51] A. Krizhevsky, I. Sutskever, and G. E. Hinton, "Imagenet classification with deep convolutional neural networks," *Adv. Neural Inform. Process. Syst.*, vol. 25, pp. 1097–1105, 2012.

[52] K. Simonyan and A. Zisserman, "Very deep convolutional networks for large-scale image recognition," *arXiv preprint arXiv:1409.1556*, 2014.

[53] C. Szegedy, W. Liu, Y. Jia, P. Sermanet, S. Reed, D. Anguelov, D. Erhan, V. Vanhoucke, and A. Rabinovich, "Going deeper with convolutions," in *IEEE Conf. Comput. Vis. Pattern Recog.*, 2015, pp. 1–9.

[54] G. Huang, Z. Liu, L. Van Der Maaten, and K. Q. Weinberger, "Densely connected convolutional networks," in *IEEE Conf. Comput. Vis. Pattern Recog.*, 2017, pp. 4700–4708.

[55] S.-H. Gao, M.-M. Cheng, K. Zhao, X.-Y. Zhang, M.-H. Yang, and P. Torr, "Res2Net: A new multi-scale backbone architecture," *IEEE Trans. Pattern Anal. Mach. Intell.*, vol. 43, no. 2, pp. 652–662, 2019.

[56] H. Zhang, C. Wu, Z. Zhang, Y. Zhu, H. Lin, Z. Zhang, Y. Sun, T. He, J. Mueller, R. Manmatha *et al.*, "ResNeSt: Split-attention networks," in *IEEE Conf. Comput. Vis. Pattern Recog.*, 2022, pp. 2736–2746.

[57] J. Hu, L. Shen, and G. Sun, "Squeeze-and-excitation networks," in *IEEE Conf. Comput. Vis. Pattern Recog.*, 2018, pp. 7132–7141.

[58] X. Li, W. Wang, X. Hu, and J. Yang, "Selective kernel networks," in *IEEE Conf. Comput. Vis. Pattern Recog.*, 2019, pp. 510–519.

[59] Z. Liu, H. Mao, C.-Y. Wu, C. Feichtenhofer, T. Darrell, and S. Xie, "A convnet for the 2020s," in *IEEE Conf. Comput. Vis. Pattern Recog.*, 2022, pp. 11 976–11 986.

[60] X. Ding, X. Zhang, J. Han, and G. Ding, "Scaling up your kernels to 31x31: Revisiting large kernel design in CNNs," in *IEEE Conf. Comput. Vis. Pattern Recog.*, 2022, pp. 11 963–11 975.

[61] S. Liu, T. Chen, X. Chen, X. Chen, Q. Xiao, B. Wu, M. Pechenizkiy, D. Mocanu, and Z. Wang, "More convnets in the 2020s: Scaling up kernels beyond 51x51 using sparsity," *arXiv preprint arXiv:2207.03620*, 2022.

[62] J. Wang, K. Sun, T. Cheng, B. Jiang, C. Deng, Y. Zhao, D. Liu, Y. Mu, M. Tan, X. Wang *et al.*, "Deep high-resolution representation learning for visual recognition," *IEEE Trans. Pattern Anal. Mach. Intell.*, vol. 43, no. 10, pp. 3349–3364, 2020.

[63] A. Vaswani, N. Shazeer, N. Parmar, J. Uszkoreit, L. Jones, A. N. Gomez, Ł. Kaiser, and I. Polosukhin, "Attention is all you need," in *Adv. Neural Inform. Process. Syst.*, 2017, pp. 5998–6008.

[64] H. Touvron, M. Cord, M. Douze, F. Massa, A. Sablayrolles, and H. Jégou, "Training data-efficient image transformers & distillation through attention," in *Int. Conf. Mach. Learn.* PMLR, 2021, pp. 10 347–10 357.

[65] L. Yuan, Y. Chen, T. Wang, W. Yu, Y. Shi, F. E. Tay, J. Feng, and S. Yan, "Tokens-to-token ViT: Training vision transformers from scratch on ImageNet," in *Int. Conf. Comput. Vis.*, 2021, pp. 558–567.

[66] H. Wu, B. Xiao, N. Codella, M. Liu, X. Dai, L. Yuan, and L. Zhang, "CvT: Introducing convolutions to vision transformers," in *Int. Conf. Comput. Vis.*, 2021, pp. 22–31.

[67] X. Chu, Z. Tian, B. Zhang, X. Wang, X. Wei, H. Xia, and C. Shen, "Conditional positional encodings for vision transformers," in *Int. Conf. Learn. Represent.*, 2023.

[68] D. Zhou, Z. Yu, E. Xie, C. Xiao, A. Anandkumar, J. Feng, and J. M. Alvarez, "Understanding the robustness in vision transformers," in *Int. Conf. Mach. Learn.* PMLR, 2022, pp. 27 378–27 394.

[69] W. Yu, M. Luo, P. Zhou, C. Si, Y. Zhou, X. Wang, J. Feng, and S. Yan, "Metaformer is actually what you need for vision," in *IEEE Conf. Comput. Vis. Pattern Recog.*, 2022, pp. 10 819–10 829.

[70] Z. Xia, X. Pan, S. Song, L. E. Li, and G. Huang, "Vision transformer with deformable attention," in *IEEE Conf. Comput. Vis. Pattern Recog.*, 2022, pp. 4794–4803.

[71] Y. Liu, Y.-H. Wu, G. Sun, L. Zhang, A. Chhatkuli, and L. Van Gool, "Vision transformers with hierarchical attention," *Machine Intelligence Research*, vol. 21, no. 4, pp. 670–683, 2024.

[72] M.-H. Guo, T.-X. Xu, J.-J. Liu, Z.-N. Liu, P.-T. Jiang, T.-J. Mu, S.-H. Zhang, R. R. Martin, M.-M. Cheng, and S.-M. Hu, "Attention mechanisms in computer vision: A survey," *Computational visual media*, vol. 8, no. 3, pp. 331–368, 2022.

[73] W. Xu, Y. Xu, T. Chang, and Z. Tu, "Co-scale conv-attentional image transformers," in *Int. Conf. Comput. Vis.*, 2021, pp. 9981–9990.

[74] D. Hendrycks and K. Gimpel, "Gaussian error linear units (gelus)," *arXiv preprint arXiv:1606.08415*, 2016.

[75] O. Russakovsky, J. Deng, H. Su, J. Krause, S. Satheesh, S. Ma, Z. Huang, A. Karpathy, A. Khosla, M. Bernstein *et al.*, "ImageNet large scale visual recognition challenge," *Int. J. Comput. Vis.*, vol. 115, no. 3, pp. 211–252, 2015.

[76] B. Cheng, I. Misra, A. G. Schwing, A. Kirillov, and R. Girdhar, "Masked-attention mask transformer for universal image segmentation," in *IEEE Conf. Comput. Vis. Pattern Recog.*, 2022, pp. 1290–1299.

[77] I. Loshchilov and F. Hutter, "Decoupled weight decay regularization," in *Int. Conf. Learn. Represent.*, 2018.

[78] H. Touvron, M. Cord, A. Sablayrolles, G. Synnaeve, and H. Jégou, "Going deeper with image transformers," in *Int. Conf. Comput. Vis.*, 2021, pp. 32–42.

[79] L. Zhu, B. Liao, Q. Zhang, X. Wang, W. Liu, and X. Wang, "Vision mamba: Efficient visual representation learning with bidirectional state space model," in *Int. Conf. Mach. Learn.*, 2024, pp. 62 429–62 442.

[80] R. Ranftl, A. Bochkovskiy, and V. Koltun, "Vision transformers for dense prediction," in *Int. Conf. Comput. Vis.*, 2021, pp. 12 179–12 188.

[81] M. Ding, B. Xiao, N. Codella, P. Luo, J. Wang, and L. Yuan, "Davit: Dual attention vision transformers," in *Eur. Conf. Comput. Vis.* Springer, 2022, pp. 74–92.

[82] A. Hatamizadeh, G. Heinrich, H. Yin, A. Tao, J. M. Alvarez, J. Kautz, and P. Molchanov, "FasterViT: Fast vision transformers with hierarchical attention," in *Int. Conf. Learn. Represent.*, 2024.

[83] W. Wang, J. Dai, Z. Chen, Z. Huang, Z. Li, X. Zhu, X. Hu, T. Lu, L. Lu, H. Li *et al.*, "Internimage: Exploring large-scale vision foundation models with deformable convolutions," in *IEEE Conf. Comput. Vis. Pattern Recog.*, 2023, pp. 14 408–14 419.

[84] J. L. Ba, J. R. Kiros, and G. E. Hinton, "Layer normalization," *arXiv preprint arXiv:1607.06450*, 2016.

[85] A. Shrivastava, A. Gupta, and R. Girshick, "Training region-based object detectors with online hard example mining," in *IEEE Conf. Comput. Vis. Pattern Recog.*, 2016, pp. 761–769.

[86] T. Xiao, Y. Liu, B. Zhou, Y. Jiang, and J. Sun, "Unified perceptual parsing for scene understanding," in *Eur. Conf. Comput. Vis.*, 2018, pp. 418–434.

[87] Y. Li, C.-Y. Wu, H. Fan, K. Mangalam, B. Xiong, J. Malik, and C. Feichtenhofer, "MViTv2: Improved multiscale vision transformers for classification and detection," in *IEEE Conf. Comput. Vis. Pattern Recog.*, 2022, pp. 4804–4814.

[88] I. Radosavovic, R. P. Kosaraju, R. Girshick, K. He, and P. Dollár, "Designing network design spaces," in *IEEE Conf. Comput. Vis. Pattern Recog.*, 2020, pp. 10 428–10 436.

[89] J. Yang, C. Li, and J. Gao, "Focal modulation networks," *arXiv preprint arXiv:2203.11926*, 2022.

[90] J. Jain, A. Singh, N. Orlov, Z. Huang, J. Li, S. Walton, and H. Shi, "Semask: Semantically masked transformers for semantic segmentation," in *International Conference on Computer Vision Workshops*, 2023, pp. 752–761.

[91] X. Lai, Z. Tian, Y. Chen, Y. Li, Y. Yuan, S. Liu, and J. Jia, "LISA: Reasoning segmentation via large language model," in *IEEE Conf. Comput. Vis. Pattern Recog.*, 2024, pp. 9579–9589.

[92] A. Radford, J. W. Kim, C. Hallacy, A. Ramesh, G. Goh, S. Agarwal, G. Sastry, A. Askell, P. Mishkin, J. Clark *et al.*, "Learning transferable visual models from natural language supervision," in *Int. Conf. Mach. Learn.* PmLR, 2021, pp. 8748–8763.

[93] H. Liu, C. Li, Q. Wu, and Y. J. Lee, "Visual instruction tuning," in *Adv. Neural Inform. Process. Syst.*, 2023, pp. 34 892–34 916.

[94] J. Li, Y. Huang, M. Wu, B. Zhang, X. Ji, and C. Zhang, "CLIP-SP: Vision-language model with adaptive prompting for scene parsing," *Computational Visual Media*, vol. 10, no. 4, pp. 741–752, 2024.

[95] T.-Y. Lin, M. Maire, S. Belongie, J. Hays, P. Perona, D. Ramanan, P. Dollár, and C. L. Zitnick, "Microsoft coco: Common objects in context," in *Eur. Conf. Comput. Vis.* Springer, 2014, pp. 740–755.

[96] S. Kazemzadeh, V. Ordonez, M. Matten, and T. Berg, "Referitgame: Referring to objects in photographs of natural scenes," in *Proceedings of the 2014 conference on empirical methods in natural language processing*, 2014, pp. 787–798.

[97] J. Mao, J. Huang, A. Toshev, O. Camburu, A. L. Yuille, and K. Murphy, "Generation and comprehension of unambiguous object descriptions," in *IEEE Conf. Comput. Vis. Pattern Recog.*, 2016, pp. 11–20.